A Real-Time Open-Circuit Fault Diagnosis Method Based on Hybrid Model Flux Observer for Voltage Source Inverter Fed Sensorless Vector Controlled Drives

Naizhe Diao, *Member, IEEE*, Yingwei Zhang, *Senior Member, IEEE*, Xianrui Sun, *Graduate Student Member, IEEE*, Chonghui Song, *Member, IEEE*, Wenwen Wang, and Haifeng Zhang, *Student Member, IEEE*

***Abstract*—This article presents a open-circuit fault diagnosis method for a sensorless vector control system based on the voltage–current hybrid model flux observer. The error voltage, which is obtained after a PI module, is used as a diagnostic factor. This PI module is designed to correct the deviation between the voltage model flux observer and the current model flux observer. The error voltage is not affected by load and speed variation. First, the activation function is used to separate fault information and normal information, and the feature function is defined to describe the signal feature in healthy and faulty conditions. Second, a second-order moving mean filtering method is proposed to reduce the storage of the error voltage data and increase the timeliness of diagnosis. Finally, the fault is diagnosed and located through logical calculations. Compared with conventional methods, this method features the timeliness of fault diagnosis in a closed-loop system and robustness with respect to speed and load changes. It reduces the storage and operation burden such that it can be easily implanted into the control algorithm as a subroutine. Simulations and experiments show the accuracy and superiority of the proposed fault diagnosis method for voltage source inverter fed sensorless vector controlled drives.**

***Index Terms*—Activation function, error voltage, fault diagnosis, hybrid model flux observer, second-order moving mean filter (SOMMF), sensorless vector control (SVC).**

I. Introduction

VOLTAGE source inverter (VSI) has been widely used in motor drives and power systems for its excellent performance, and its reliability is very important to industrial safety production [1], [2], [3]. In industrial applications, the open-circuit (OC) fault of an inverter is one of the main faults of the inverter [4], [5]. The OC fault leads to current distortion, which can generate secondary faults such as other healthy switches reaching breakdown. More than this, it will make the entire system to be shut down and cause serious economic losses [6], [7]. Therefore, if the OC fault can be found and diagnosed in time, it can be repaired in time without causing greater losses.

Due to the wide application of vector control technology, the switch OC fault diagnosis in the closed-loop system needs more research. In the vector control closed-loop system, when one of the power switches of some phase is a fault, part of this phase current will be lost. Due to the current closed-loop regulator, the current characteristics in the vector control drive system are much more complicated than the open-loop control motor drive system. The vector control system maintains the circular motion of the flux field by increasing or decreasing the dc component of the other phase currents. At this time, some fault diagnosis methods [9], [10], [11], [12], [13], [14], [15], [16] of open-loop control will not be applicable [8]. These current-based methods have good performance in open-loop control methods such as the V/f control strategy, but they are not very effective in closed-loop control methods.

Fast fault diagnosis methods based on voltage had been proposed in [17], [18], [19], [20], [21], [22], and [23]. With these voltage-based methods, the OC faults can be detected as quickly as possible within one or several switching cycles. However, these additional ultrahigh-speed sampling circuits needed in these voltage-based methods are their main disadvantages, since it increases the cost, the design complexity, and the point of failure of the system.

In recent years, the model-based fault diagnosis method based on the observer has been a hot spot. In [24], the OC faults method under closed-loop operation are proposed based on the variable structure observers. The method used the residual signals for fault isolation. So the method performs well with relatively short detection time in vector control algorithms. The work [25] used

Manuscript received 18 May 2022; revised 19 August 2022; accepted 9 October 2022. Date of publication 25 October 2022; date of current version 18 November 2022. This work was supported in part by the National Key R&D Program of China under Grant 2022YFE0102500, in part by the National Natural Science Foundation of China under Grant 61773006, and in part by the Nature Science Foundation of Liaoning Province under Grant 2022JH/6100100022 Recommended for publication by Associate Editor J. Hur. *(Corresponding author: Chonghui Song.)*

Naizhe Diao is with the College of Electrical Engineering, Yanshan University, Qinhuangdao 066004, China (e-mail: diaonaizhe@163.com).

Yingwei Zhang, Xianrui Sun, Chonghui Song, Wenwen Wang, and Haifeng Zhang are with the College of Information Science and Engineering, Northeastern University, Shenyang 110819, China (e-mail: zhangyingwei@ise.neu.edu.cn; xianruisun@163.com; chonghui.song@gmail.com; 1970533@stu.neu.edu.cn; haif_zh@163.com).

Color versions of one or more figures in this article are available at https://doi.org/10.1109/TPEL.2022.3216870.

Digital Object Identifier 10.1109/TPEL.2022.3216870

nonlinear Luenberger state observer plus a directional evaluation to detect and isolate switch faults based on the induction motor (IM) model. However, since they are based on residuals, they are very sensitive to changes in motor parameters. The threshold setting is very sensitive, which will affect the robustness and reliability of the diagnostic method. The work [26] used the observed data to compute the value of the current factor and compared it with model data. Adaptive thresholds are used to detect fault results. In [27], a multiclass neural network has been proposed to detect and isolate a single switch OC fault in a closed-loop system. The work [28] proposed an OC fault diagnosis method based on three-phase current distortions in VSIs for vector-controlled induction motor drives. It calculated the synchronously rotating angle to locate the fault, which is by a lookup table (LUT) that consists of faulty state and normal state. However, it is sensitive to the parameter uncertainty and unmodeled dynamics, which is not constant during the different state. The use of allelic point functions was proposed in [29]; it showed fast detection and good performance related to single or multiple OC faults in the closed-loop system. However, it did not perform very well in the transient process and was prone to false alarms.

In addition, most of them adopt periodic features to diagnosis fault [25], [26], [27], [29], [30], [31]. Due to the higher sampling frequency data, the periodic fault diagnosis needs to record many sampling data to drive the fault diagnosis algorithm. It causes the algorithm to calculate more than 200 times in a cycle time, and the computed data are more than 3×200 points every time. Therefore, these related algorithms are of high complexity. The higher complexity leads to a higher calculation burden and wastes corresponding memory space and diagnosis time. Therefore, it is further necessary to research the fault diagnosis algorithm for the inverter to improve the practicality.

To accurately diagnose OC faults under variable-speed and variable-load conditions in the sensorless vector control (SVC) system without additional hardware, this article proposes an OC fault diagnosis method based on a hybrid model flux observer. The main contributions of this article are summarized as follows.

1) The error voltage is used as a diagnostic factor. It has a large deviation between fault condition and normal condition and it is not affected by speed changes and load changes. At the same time, it does not increase the hardware requirements.
2) The activation function is proposed. It can separate the fault information and normal information as much as possible so that the fault characteristics are more obvious.
3) The second-order moving mean filtering (SOMMF) method is proposed. SOMMF can greatly reduce the amount of calculation and storage, which also greatly reduces the calculation time of the characteristic function, so as to achieve fast diagnosis. It can make the proposed method more effective in practical applications.

The remainder of this article is organized as follows. Section II analyzes the OC fault of the inverter in a closed-loop system using the hybrid model flux observer. Section III proposes a method based on the hybrid model flux observer to diagnose the switch OC faults. Section IV verifies the correctness of the diagnostic method through simulation and experiments. Section V concludes the article.

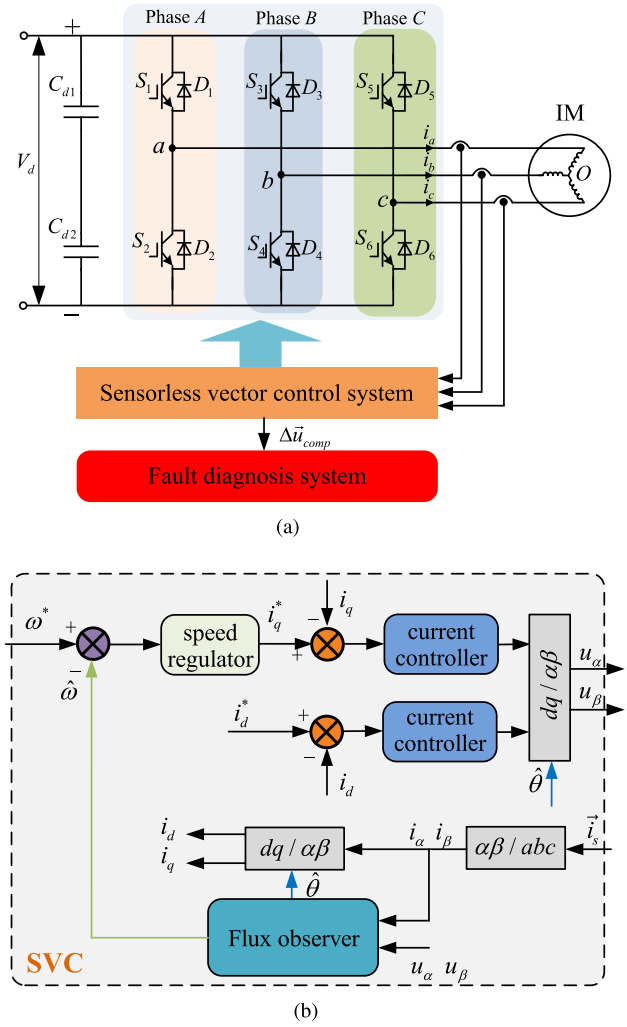

Fig. 1. Sensorless vector control system of an induction motor.

II. OC Fault Analysis Based on Hybrid Model Flux Observer

A. Sensorless Vector Control Drive System

Fig. 1 shows the structure of the two-level inverter fed sensorless vector controlled drives. The inverter consists of six switches (S_1–S_6) with six antiparallel diodes (D_1–D_6). i_a, i_b, and i_c are three-phase phase currents. V_d is the dc bus voltage.

In the SVC system, the rotor flux angle and speed are estimated by the flux observer. Then, the stator current is decomposed through coordinate transformation into two synchronously rotating vector components i_d and i_q, which are independently controlled to control the rotor flux and torque, respectively. The reference speed and estimated speed of the induction motor are applied to SVC to generate pulsewidth modulation driving signals to control the turn-ON and turn-OFF of the insulated gate bipolar transistors (IGBTs).

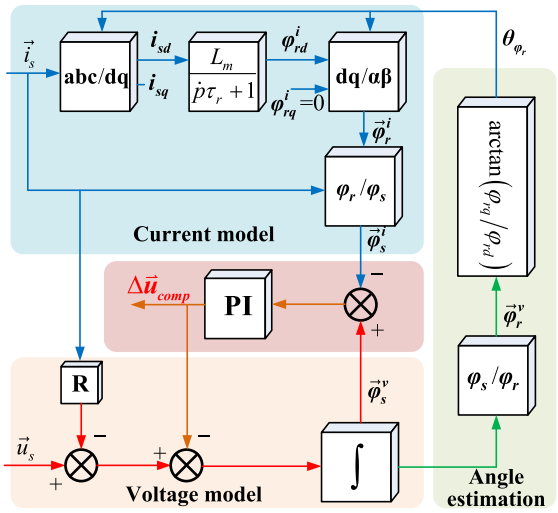

Fig. 2. Hybrid model rotor flux observer.

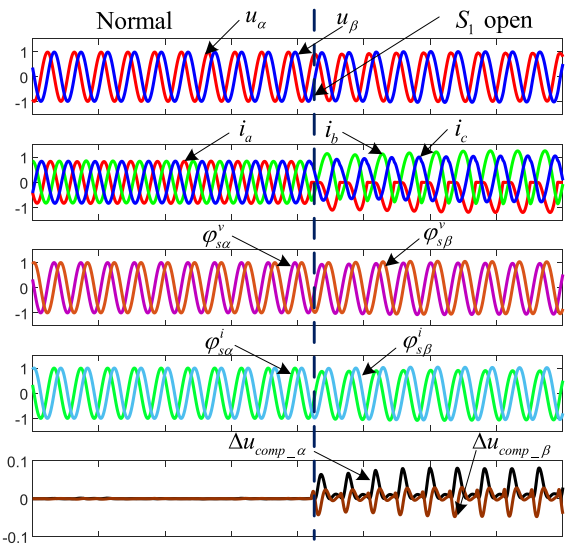

Fig. 3. Three-phase currents, $\alpha\beta$ voltages, and error voltages in the SVC when S_1 occurs fault.

The fault diagnosis system is independent of the vector control system, which only uses the error voltage as the diagnosis factor. The two diagnosis signal "fault flag" and "fault variables" are used for fault detection and fault location, respectively.

B. Definition of Error Voltage in Hybrid Model Flux Observer

Define some symbols. $\vec{\varphi}_s^v = \varphi_{s\alpha}^v + j\varphi_{s\beta}^v$ is the stator flux estimated by the voltage model flux observer. $\vec{\varphi}_s^i = \varphi_{s\alpha}^i + j\varphi_{s\beta}^i$ is the stator flux estimated by the current model flux observer. $\vec{u}_s = u_\alpha + ju_\beta$ is the output phase voltage vector. $\vec{i}_s$ is the output phase current vector. R_s is the stator resistance. τ_r is the rotor time constant. L_s is the stator inductance. L_r is the stator inductance. L_m is the magnetizing inductance. θ_{φ_r} is the rotor flux angle. $\dot{p}$ is the derivative operator ($\dot{p} = d/dt$).

In the SVC system, a voltage–current hybrid model flux observer [32], [33] is shown in Fig. 2.

In the current model, the rotor flux $\vec{\varphi}_r^i$ is the same with the rotor flux in the d-axis φ_{rd}^i due to the rotor field orientation

$$\begin{cases} \varphi_{rd}^i = \frac{L_m}{\dot{p}\tau_r + 1} i_{sd}, \\ \varphi_{rq}^i = 0 \end{cases} \tag{1}$$

where φ_{rd}^i and φ_{rq}^i can be transformed to $\varphi_{r\alpha}^i$ and $\varphi_{r\beta}^i$ in the stationary reference frame, i.e.,

$$\begin{bmatrix} \varphi_{r\alpha}^i \\ \varphi_{r\beta}^i \end{bmatrix} = \begin{bmatrix} \cos\theta_{\varphi_r} & -\sin\theta_{\varphi_r} \\ \sin\theta_{\varphi_r} & \cos\theta_{\varphi_r} \end{bmatrix} \begin{bmatrix} \varphi_{rd}^i \\ \varphi_{rq}^i \end{bmatrix}. \tag{2}$$

Then, in the stator reference frame, $\vec{\varphi}_s^i = \varphi_{s\alpha}^i + \varphi_{s\beta}^i$ is computed from $\varphi_{r\alpha}^i$ and $\varphi_{r\beta}^i$ by

$$\begin{cases} \varphi_{s\alpha}^i = \frac{L_s L_r - L_m^2}{L_r} i_{s\alpha} + \frac{L_m}{L_r} \varphi_{r\alpha}^i \\ \varphi_{s\beta}^i = \frac{L_s L_r - L_m^2}{L_r} i_{s\beta} + \frac{L_m}{L_r} \varphi_{r\beta}^i \end{cases}. \tag{3}$$

Next, in the voltage model, $\vec{\varphi}_s^v = \varphi_{s\alpha}^v + j\varphi_{s\beta}^v$ is calculated by means of the back electromotive force's integration

$$\begin{cases} \varphi_{s\alpha}^v = \int (u_\alpha - i_{s\alpha} R_s) dt \\ \varphi_{s\beta}^v = \int (u_\beta - i_{s\beta} R_s) dt \end{cases}. \tag{4}$$

Since pure integration will cause the error effect due to the noise or the sampling error. To compensate for the errors caused by the pure integrator, the compensation voltage $\Delta\vec{u}_{\text{comp}}$ is generated by the PI module [34]

$$\begin{cases} \Delta u_{\text{comp}\_\alpha} = k_p \left(\varphi_{s\alpha}^v - \varphi_{s\alpha}^i\right) + \frac{k_i}{s} \left(\varphi_{s\alpha}^v - \varphi_{s\alpha}^i\right) \\ \Delta u_{\text{comp}\_\beta} = k_p \left(\varphi_{s\beta}^v - \varphi_{s\beta}^i\right) + \frac{k_i}{s} \left(\varphi_{s\beta}^v - \varphi_{s\beta}^i\right) \end{cases} \tag{5}$$

where k_p is the proportional coefficient and k_i is the integral coefficient.

So (4) can be rewritten as

$$\begin{cases} \varphi_{s\alpha}^v = \int (u_\alpha - i_{s\alpha} R_s - \Delta u_{\text{comp}\_\alpha}) dt \\ \varphi_{s\beta}^v = \int (u_\beta - i_{s\beta} R_s - \Delta u_{\text{comp}\_\beta}) dt \end{cases}. \tag{6}$$

Then, the rotor flux based on voltage model is further computed as

$$\begin{cases} \varphi_{r\alpha}^v = -\frac{L_s L_r - L_m^2}{L_m} i_{s\alpha} + \frac{L_r}{L_m} \varphi_{s\alpha}^v \\ \varphi_{r\beta}^v = -\frac{L_s L_r - L_m^2}{L_m} i_{s\beta} + \frac{L_r}{L_m} \varphi_{s\beta}^v \end{cases}. \tag{7}$$

Finally, the rotor flux angle based on the voltage model is computed as

$$\theta_{\varphi_r} = \tan^{-1} \left(\frac{\varphi_{r\beta}^v}{\varphi_{r\alpha}^v} \right). \tag{8}$$

Then the torque and the flux component used in the SVC can be obtained.

C. Analysis Inverter Normal and Faulty Conditions Based on the Error Voltage

In the SVC system adopting the hybrid model flux observer, three-phase currents, $\alpha\beta$ voltages, and error voltages are shown in Fig. 3. In normal conditions, $\Delta\vec{u}_{\text{comp}}$ is close to zero. However, when S_1 occurs the OC fault, i_s has an obvious distortion. Then, in the current model, $\vec{\varphi}_s^i$ is consistent with the actual situation because it is calculated by the current signal. However, in the voltage model, $\vec{u}_s$ is usually the reference voltage or the

voltage reconstructed from the internal signal [33], rather than the voltage obtained by an external hardware circuit. Since it is not affected by the OC fault, the result is that $\vec{u}_s - \vec{i}_s R_s$ would deviate from the actual situation. In this way, $\vec{\varphi}_s^v$ will not match $\vec{\varphi}_s^i$, and the deviation would be delivered to $\Delta\vec{u}_{\text{comp}}$ after the PI module. Hence, $\Delta\vec{u}_{\text{comp}}$ is chosen to monitor the inverter's state, whether it is normal or faulty, in the closed-loop system.

III. Proposed Fault Diagnosis Method

This article proposes a real-time OC fault diagnosis method based on the voltage–current hybrid model flux observer in the SVC system. The method uses $\Delta\vec{u}_{\text{comp}}$ after the PI compensation model for the OC fault diagnosis. Here, $\Delta\vec{u}_{\text{comp}} = \Delta u_{\text{comp}\_\alpha} + j\Delta u_{\text{comp}\_\beta}$.

A. Error Voltage Feature Extraction

In the normal condition, although $\vec{\varphi}_s^v$ and $\vec{\varphi}_s^i$ are estimated by different observers, they both describe the same variable $\vec{\varphi}_s$ in the system. Hence, $\vec{\varphi}_s^v$, $\vec{\varphi}_s^i$, and $\vec{\varphi}_s$ are almost equal, i.e.,

$$\vec{\varphi}_s^v \approx \vec{\varphi}_s^i \approx \vec{\varphi}_s. \tag{9}$$

Then, (5) can be simplified to

$$\Delta\vec{u}_{\text{comp}} = \mathbf{PI}\left(\vec{\varphi}_s^v - \vec{\varphi}_s^i\right) \approx 0 \tag{10}$$

where $\mathbf{PI}(\cdot)$ denotes the PI regulation process.

The error between $\vec{\varphi}_s^v$ and $\vec{\varphi}_s^i$ can be caused by pure integral sampling error; so they are not affected by other factors such as torque and speed changes. Therefore, in the normal condition, $\vec{\varphi}_s^v$ and $\vec{\varphi}_s^i$ are only slightly different.

However, in the faulty condition, $\vec{\varphi}_s^v$ would deviate from $\vec{\varphi}_s$ according to (6) since $\vec{u}_s$ is still using the reference voltage. But $\vec{\varphi}_s^i$ is still approximately equal to $\vec{\varphi}_s$ according to (5)

$$\vec{\varphi}_s^v \neq \vec{\varphi}_s^i \approx \vec{\varphi}_s. \tag{11}$$

At this time, $\vec{\varphi}_s^v$ and $\vec{\varphi}_s^i$ would generate a large fluctuation and the fluctuations are transferred to $\Delta\vec{u}_{\text{comp}}$ after the PI module

$$\Delta\vec{u}_{\text{comp}} = \mathbf{PI}\left(\vec{\varphi}_s^v - \vec{\varphi}_s^i\right) \not\approx 0. \tag{12}$$

Since $\Delta\vec{u}_{\text{comp}}$ is obviously different in normal and faulty conditions, it is selected as the diagnostic factor. Because it is not affected by changes in torque and speed, it can fit for variable-speed and variable-load conditions.

To locate the fault switch, $\Delta\vec{u}_{\text{comp}}$ is transformed into three-phase error voltages $e^p, p = a, b, c$ by (13). Here, a, b, and c represent phases A, B, and C, respectively

$$\begin{bmatrix} e^a \\ e^b \\ e^c \end{bmatrix} = \begin{bmatrix} \Delta u_{\text{comp}\_\alpha} \\ -\frac{1}{2}\Delta u_{\text{comp}\_\alpha} + \frac{\sqrt{3}}{2}\Delta u_{\text{comp}\_\beta} \\ -\frac{1}{2}\Delta u_{\text{comp}\_\alpha} - \frac{\sqrt{3}}{2}\Delta u_{\text{comp}\_\beta} \end{bmatrix}. \tag{13}$$

According to the previous analysis, $e^p \approx 0$ under normal conditions. While the OC fault occurs, e^p deviates from 0 and becomes obviously positive or negative. Considering the robustness to transient states caused by torque and speed changes, the activation function is adopted to enlarge the difference under normal and fault conditions

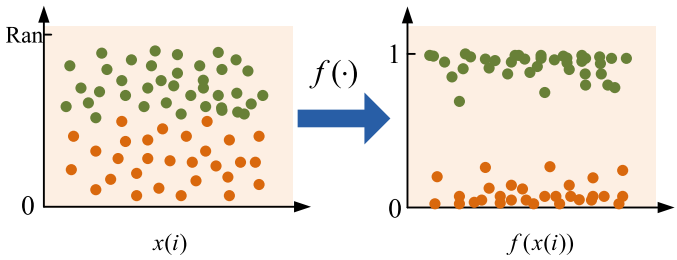

Fig. 4. Role of activation function.

$$X^p(i) = f\left(e^p(i)\right) \tag{14}$$

where $f(\cdot)$ is the activation function and i is the discrete sampling time. $f(\cdot)$ can make the error voltage close to 0 in normal conditions and close to 1 or –1 in faulty conditions, as shown in Fig. 4.

For example

$$f(x) = \begin{cases} 0, & \text{if } |x| \le K_1, \\ 1, & \text{if } x > K_1, \\ -1, & \text{if } x < -K_1 \end{cases} \tag{15}$$

where K_1 is a threshold.

Generally, during the transient process such as torque changes or variable speed, the error voltage will also change; however, the value of the error voltage will always remain near zero when no fault occurs. Then, in the normal state, the error voltage will sustain long intervals close to zero. Each error voltage sample can be classified as close to zero using $f(\cdot)$. When a fault occurs, the error voltage would deviate from the value close to zero. Then the error voltage sample can be classified as 1 or –1 using $f(\cdot)$.

Therefore, $f(\cdot)$ not only makes the fault information more obvious but also weakens the periodic characteristics of the signal.

Remark 1: The $\tanh(\cdot)$ function can also be used as $f(\cdot)$

$$f(x) = \tanh\left(K_2 x\right) = \frac{e^{K_2 x} - e^{-K_2 x}}{e^{K_2 x} + e^{-K_2 x}} \tag{16}$$

where K_2 is a parameter that is used to control the speed at which the data tends to the target value.

However, $X^p(i)$ still cannot be directly applied to describe the signal feature due to its irregular change. So a specified period mean value method is proposed to extract the fault feature. S_k^p is defined to describe the points at the discrete time k constructed by the three-phase error voltages in the specified period

$$S^p(k) = [X^p(k-N), X^p(k-N+1), \ldots, X^p(k)] \tag{17}$$

where N is the number of sampling points in the specified period T, and

$$N = T \times f_s \tag{18}$$

where f_s is the sampling frequency of the error voltage.

The feature function $P^p(k)$ can be expressed as

$$P^p(k) = \frac{1}{N}\sum_{i=1}^{N} S_i^p(k) \tag{19}$$

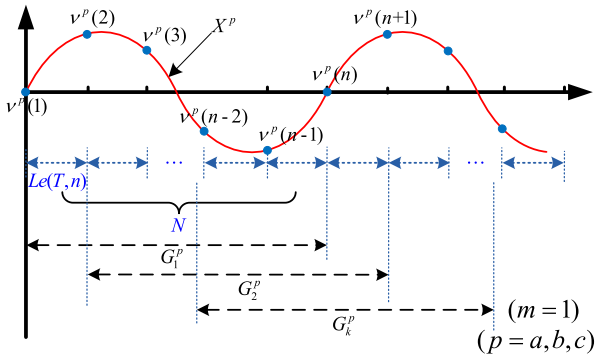

Fig. 5. Second-order moving mean filtering method.

where i is the ith element of $S^p(k)$.

To avoid the huge amount of calculation caused by computing at each sampling point, the sliding step of S_k^p is set to h

$$S^p(k+1) = [X^p(k+h-N), \ldots, X^p(k+h)]. \tag{20}$$

$$P^p(k+1) = \frac{1}{N}\sum_{i=1}^{N} S_i^p(k+1). \tag{21}$$

Equations (19) and (21) are called the direct moving mean filter (DMMF). $S^p(k)$ continuously collects new sampling points while discarding part of the old data when calculating $P^p(k)$. It requires a cycle of data to be stored in real time. If $S^p(k)$ has many dimensions and the sampling frequency is high, it will take up a lot of storage burden.

B. Second-Order Moving Mean Filter

In an actual system, the calculation of periodic characteristics also takes time, especially at low speeds, and when the sampling frequency is high, the acquisition of periodic characteristics requires tens of thousands of data to participate in the calculation by DMMF. This will take up a lot of interruption time in the micro controller unit (MCU), leading to the paralysis of the system.

In order to have sufficiently high accuracy and low complexity, the SOMMF method is proposed, as shown in Fig. 5.

In T, sampling points can be divided into n subspaces. The number of sampling points in each subspace is

$$Le(T,n) = \text{Round}\left(\frac{f_s \times T}{n}\right). \tag{22}$$

The jth subspace $D^p(j), j = 1, \ldots, n$ is

$$D^p(j) = [X^p((j-1)Le(T,n)+1), \ldots, X^p(j \times Le(T,n))]. \tag{23}$$

The average processing is

$$\nu^p(j) = \frac{1}{Le(T,n)+1}\sum_{i=0}^{Le(T,n)} D_i^p(j). \tag{24}$$

$\nu^p(j)$ represents the feature of the jth subspace.

In the kth sampling step, the new dataset $G^p(k)$, composed of $\nu^p(j), (k-1)h - n < j \le (k-1)h$, instead of $S^p(k)$ that

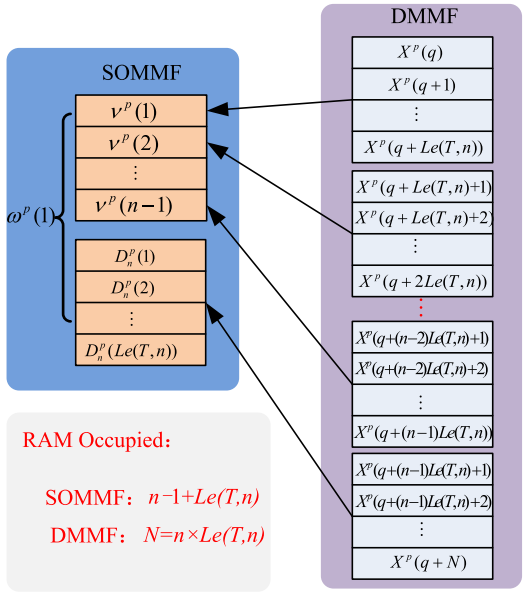

Fig. 6. Comparison of memory usage between SOMMF and DMMF.

is composed of $X^p(i), k-N < i \le k$, is

$$G^p(k) = [\nu^p(k-1)h, \nu^p((k-1)h-1), \ldots, \nu^p((k-1)h-n)]. \tag{25}$$

The feature function $Q^p(k)$ of $G^p(k)$ is

$$Q^p(k) = \frac{1}{n+1}\sum_{i=1}^{n} G_i^p(k). \tag{26}$$

Equations (23)–(26) define a new process called the SOMMF method.

Because $P^p(k)$ and $Q^p(k)$ both calculate the feature of $S^p(k)$, they are the same even though the calculated paths are different, i.e.,

$$P^p(k) = Q^p(k). \tag{27}$$

Remark 2: The SOMMF method can greatly reduce the storage space and calculation burden, as shown in Fig. 6 . For 1-D data, the minimum storage and the minimum calculation times using the SOMMF in a cycle are

$$S_{\text{sto}}^{\text{SOMMF}} = \min_{n\times Le(T,n)=N}(n+Le(T,n))-1 \tag{28}$$

and

$$S_{\text{cal}}^{\text{SOMMF}} = \left(\min_{n\times Le(T,n)=N}(n+Le(T,n))\right) - Le(T,n). \tag{29}$$

The storage and the calculation times using the DMMF (19) and (21) are

$$S_{\text{sto}}^{\text{DMMF}} = S_{\text{cal}}^{\text{DMMF}} = N = n \times Le(T,n). \tag{30}$$

Since f_s is very high

$$n \times Le(T,n) \gg n + Le(T,n). \tag{31}$$

Therefore

$$S_{\text{sto}}^{\text{SOMMF}} \ll S_{\text{sto}}^{\text{DMMF}} \text{ and } S_{\text{cal}}^{\text{SOMMF}} \ll S_{\text{cal}}^{\text{DMMF}}. \tag{32}$$

Therefore, the SOMMF method will greatly reduce the storage space and calculation burden.

Remark 3: The sliding step h can be set to $h = m \times Le(T, n)$; here, m is an integer. It can simplify the SOMMF method.

C. Fault Detection

Since the error voltage is nonsinusoidal within a fundamental frequency, the mean value varies with the time when the fault occurs. Therefore, in order to detect the faults in time, $e^p(i)$ can be regularized first by

$$\bar{e}^p(i) = |e^p(i)|. \tag{33}$$

Then

$$\bar{X}^p(\cdot) = f\left(\bar{e}^p(i)\right). \tag{34}$$

Similar to (23)–(25), $\bar{D}^p(j)$ and $\bar{G}^p(k)$ are constructed by replacing the corresponding elements $\bar{X}^p(\cdot)$ in (23)–(25). $\bar{\nu}^p(j)$ and $\bar{Q}^p(k)$ are calculated by the SOMMF method, i.e.,

$$\bar{\nu}^p(j) = \frac{1}{Le(T,n)+1} \sum_{i=0}^{Le(T,n)} \bar{D}_i^p(j), \tag{35}$$

$$\bar{Q}^p(k) = \frac{1}{n+1} \sum_{i=1}^{n} \bar{G}_i^p(k). \tag{36}$$

Finally, the fault can be detected by

$$f_g = \begin{cases} 0, \text{ if } \begin{cases} \bar{Q}^a(k) < K_d, \\ \bar{Q}^b(k) < K_d, \\ \bar{Q}^c(k) < K_d, \end{cases} \\ 1, \text{ else} \end{cases} \tag{37}$$

where K_d is the logical threshold.

D. Fault Location

Due to $f(\cdot)$, $Q^p(k)$ has a distinct differentiation between fault and normal conditions. So they can be used to locate the fault. By comparing $Q^p(k)$ with the logical threshold K_l, the diagnosis variable E_k^p is obtained

$$E_k^p = \begin{cases} \text{H}, & \text{if } Q^p(k) > K_l \\ 0, & \text{if } -K_l < Q^p(k) < K_l \\ \text{L}, & \text{if } Q^p(k) < -K_l \end{cases}. \tag{38}$$

There are three kinds of outputs of E_k^p for one phase, i.e., H, 0, and L.

When 0 occurs, it represents no OC fault. When other values appear, it means that the fault is occurred. Furthermore, to locate the fault, E_k^a, E_k^b, and E_k^c are needed at the same time. For example, if $E_k^a = \text{H}$, $E_k^b = \text{L}$, and $E_k^c = \text{L}$, it represents that the OC fault of S_1 is isolated. This is because when S_1 creates an OC fault, i_a loses its positive part. Since $\vec{\varphi}_{sa}^i$ is calculated by i_a, its positive amplitude will be lower due to i_a. Then, the deviation would be delivered to $\Delta\vec{u}_{\text{comp}}$ via the PI module. Thus, the positive amplitude of e^a will increase by using (10) and (13), which results in $E_k^a = \text{H}$. At the same time, due to the loss of the positive amplitude of i_a, i_b, and i_c will increase the positive amplitude since $i_a + i_b + i_c = 0$. Thus, positive amplitudes of the $\vec{\varphi}_{sb}^i$ and $\vec{\varphi}_{sc}^i$ become larger. Due to (10) and (13), the negative amplitudes of e^b and e^c will increase, causing $E_k^b = \text{L}$ and $E_k^c = \text{L}$. Similarly, when S_2 creates an OC fault, i_a loses its negative part. The result is that the negative amplitude of e^a is increased and positive amplitudes of e^b and e^c are increased. The detailed relationship between the OC fault of each power switch and E_k^p is given in Table I.

TABLE I
RELATIONSHIP BETWEEN THE OC FAULT OF EACH POWER SWITCH AND E_k^p

Faulty switch	E_k^a	E_k^b	E_k^c
Normal	0	0	0
S_1	H	L	L
S_2	L	H	H
S_3	L	H	L
S_4	H	L	H
S_5	L	L	H
S_6	H	H	L

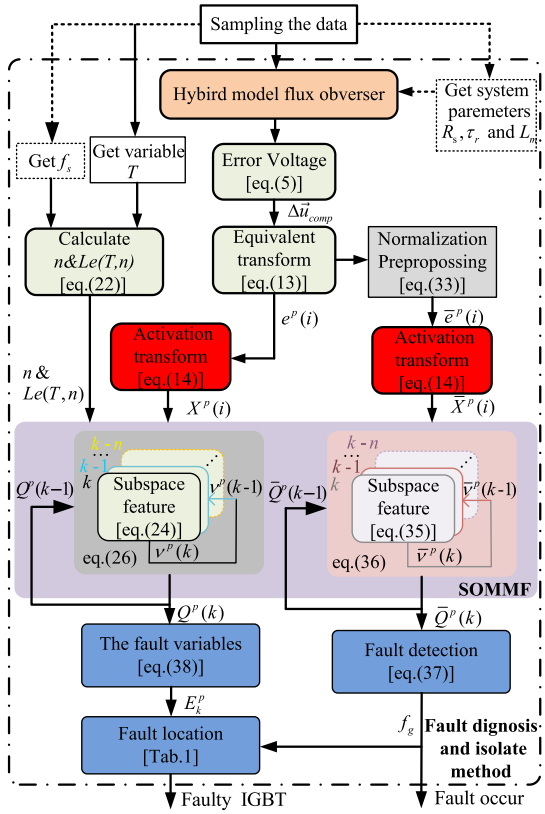

Fig. 7. Flowchart for the proposed diagnostic algorithm.

E. System Block Diagram

Fig. 7 shows a flowchart of the proposed fault diagnosis algorithm.

The error voltage is used as a diagnostic factor since it is not affected by speed changes and load changes. Then, the activation

TABLE II
VALUES OF THE PARAMETERS

Parameter	K_d	K_l	K_1	K_2
Value	0.2	0.2	0.02	50

function is used to separate the fault information and normal information as much as possible so that the fault characteristics are more obvious. Next, the fault flag f_g and the fault variables E_k^p are calculated using the SOMMF method, which can greatly reduce the amount of calculation and storage. f_g is compared with K_d to identify the faults. If $f_g > K_d$, there are OC faults. Finally, the faulty switch is located by E_k^p.

F. Parameter Determination

The proposed method needs two parameters: K_d and K_l. K_d is a threshold used for fault detection by comparing with the $\bar{Q}^p$. K_l is a threshold applied to isolate the faulty switch by comparing Q^p with it. The larger value of the parameters will reduce the chance of misjudgment caused by current noise or torque changed and increase the robustness of the system. However, it will increase the detection time. Thus, their values should be less than 0.5 considering that the proportionality of error voltage per period will be near to 0.5 when the OC fault occurs. But they must be greater than two times the error voltage period value under the normal state. K_1 is a threshold; it is used to detect whether the error voltage is close to zero or not; its value is close to zero and generally defined as 1/5–1/10 of the error voltage peak in the fault condition. K_2 is a constant parameter, which is used to separate normal and fault features. It usually converts 1/2 of the peak error voltage in the fault condition into the target value of the activation function.

The values of the parameters can be obtained by the simulation and experiment, as shown in Table II.

IV. SIMULATION AND EXPERIMENT

The effectiveness of the proposed fault diagnosis method is verified by the simulation and experiment.

A. Simulation Analysis

The SVC system based on hybrid model flux observer of the two-level inverter shown in Fig. 1 is built in MATLAB. The load is a 2.2-kW induction motor, with 4.5-A rated current, 50-Hz rated frequency, and 380-V rated voltage. $f_s = 10$ kHz. In the simulation, $T = 30$ ms, $N = 300$, $n = 20$, and $m = 1$. Equation (16) is used as the activation function. The motor, load torque change, and the variable speed are used to prove the robustness of the proposed diagnosis method.

1) Fault Diagnosis When Speed Changes: Fig. 8 shows the results with variable speed in healthy condition. The given frequency is 30 Hz. Fig. 8(a) shows three-current signals. Fig. 8(b) shows the error voltage signals. Fig. 8(c) shows the absolutely mean values. Fig. 8(d) shows the mean value. Fig. 8(e) shows the detection and isolation results for different faulty switches. From those figures, when the frequency changes, e^p has not changed much and always remains close to zero during this process. Then, the feature function does not reach K_d, which indicates that no fault has occurred. As a result, the diagnostic signals remain zero and no false alarm is issued by this condition.

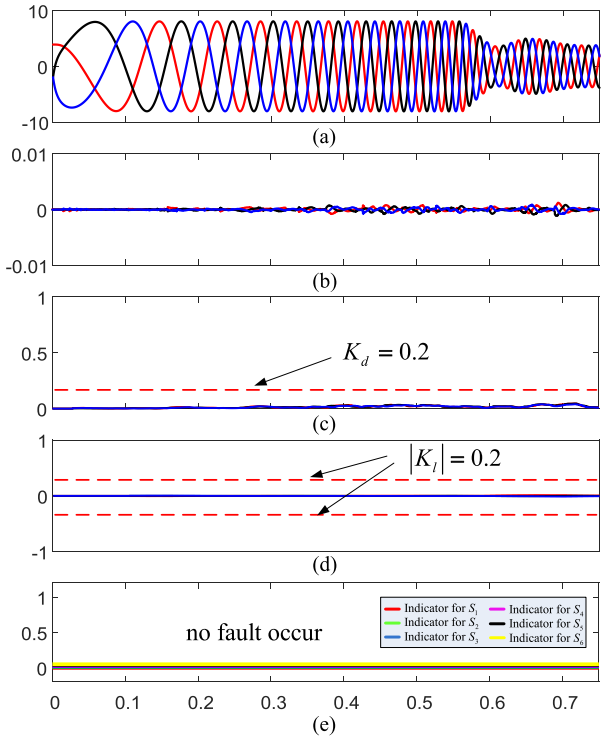

Fig. 8. Simulation results of the fault diagnosis when the given frequency is 30 Hz.

2) Fault Diagnosis When Load Change and Fault Occur: Fig. 9 shows the simulation result for the load torque and the OC fault of S_1. The load torque changes in 0.1 and 0.25 s, respectively. The S_1 OC fault is occurred at 0.4 s.

Fig. 9(a) is three-current signals. Fig. 9(b) shows error voltages in the normal conditions and fault condition. In Fig. 9(c), the periodic averages of the absolute error voltages are obtained by the SOMMF method. Fig. 9(d) shows the mean value of the error voltage with the SOMMF method. Fig. 9(e) shows the diagnosis result. As can be seen from Fig. 9, when the torque changes, there is no change in the error voltage. This shows well that the error voltage is independent of the torque change. However, when a OC fault occurs, e_p fluctuates greatly. Then the feature function $\bar{Q}^p(k)$ is quickly increased. When this value reaches K_d, f_g is triggered; so the fault signal is effectively extracted. Then, $Q^a(k)$ is quickly increased, and $Q^b(k)$ and $Q^c(k)$ are decreased. They quickly reach K_l and trigger E_k^p. Thus, S_1 OC fault is accurately detected and isolated, respectively.

3) Fault Diagnosis When Load and Speed Are Changing: Fig. 10 shows simulation results for the OC fault of S_2 with load and speed changes. The speed and load changed at 0.1 s. The S_2 OC fault occurred at 0.26 s.

Fig. 10(a) shows three-phase currents. Fig. 10(b) shows error voltages in normal conditions and the fault condition. In Fig. 10(c), the absolute feature values of the absolute error

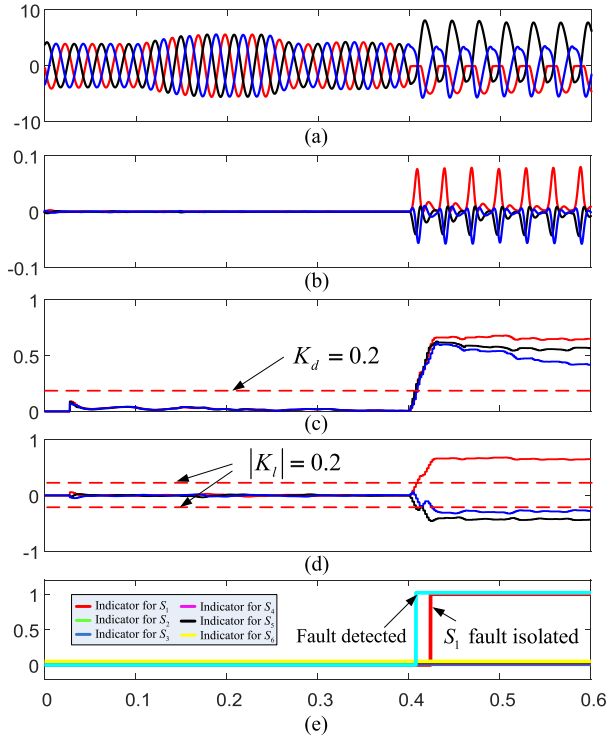

Fig. 9. Simulation results when the load torque and the OC fault occur to S_1 at 30 Hz.

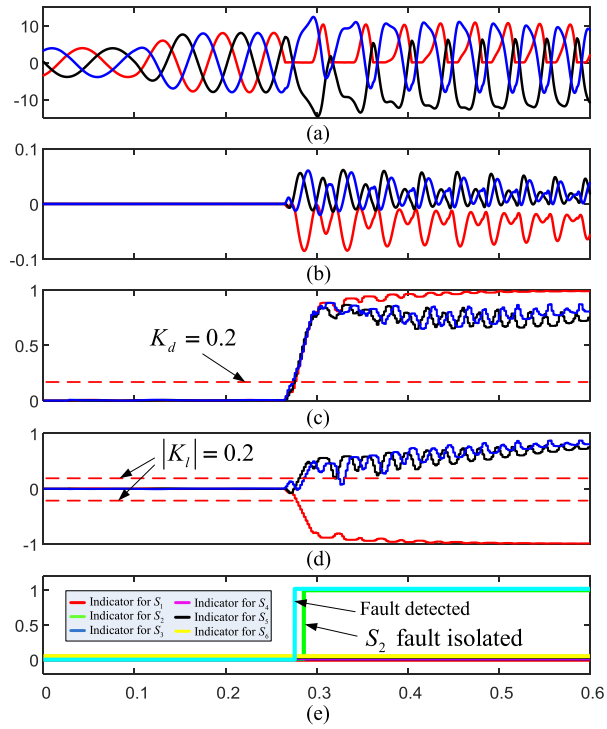

Fig. 10. Simulation results when speed and load change under OC fault occur.

voltages are obtained by the SOMMF method. Fig. 10(d) shows the mean value of the error voltage with the SOMMF method. Fig. 10(e) is the diagnosis result. From Fig. 10, when the speed and load change, the error voltage is almost unchanged. However, e_p fluctuates greatly when OC fault occurs. Then the feature function $\bar{Q}^p(k)$ is quickly increased. Although the period of the error voltage changes, the exact signal period is no longer required due to the use of the activation function. When $\bar{Q}^p(k)$ reaches K_d, f_g is triggered; so the fault signal is effectively extracted. Then, $Q^a(k)$ decreased, and $Q^b(k)$ and $Q^c(k)$ increased, and E_k^p is triggered. Thus, the S_2 OC fault is accurately detected and isolated. Therefore, changes in speed and load do not affect the correct diagnosis and location of faults.

4) Fault Diagnosis When Load and Speed Change Under Fault Occur: Fig. 11 shows the simulation result when the load changes frequently and S_3 creates the OC fault. The load changes at 0.05, 0.3, 0.4, 0.7, 0.9, and 1.1 s, respectively. S_3 creates the OC fault at 1.3 s.

From Fig. 11, the fluctuation of the error voltage caused by sharp transients such as instantaneous loading or unloading is not very obvious, and the fluctuation is even less noticeable under the periodic characteristics. However, when an OC fault occurs, e_p fluctuates greatly. After the added activation function, the fault information is amplified. Then, the S_3 OC fault is accurately detected and isolated. Therefore, during the loading or unloading process, the fault will not be falsely reported, and only when the fault occurs, the fault alarm will be triggered to locate the fault.

5) Fault Diagnosis When Motor Parameters Are Inaccurate: Most SVC systems use an LUT method to select parameters in different states, that is, LUT is a parameter curve obtained

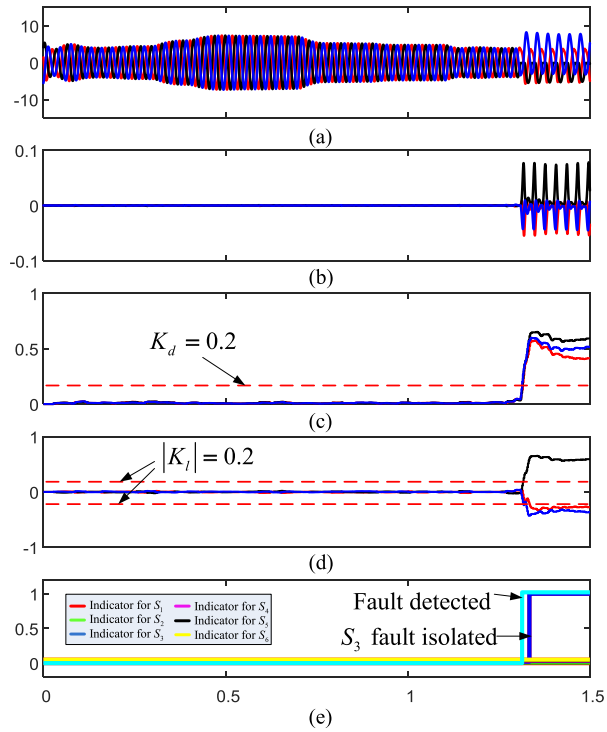

Fig. 11. Simulation results when the load changes frequently.

through offline or online identification for different operating conditions [37]. The parameter identification of the motor has been developed for decades; so the accuracy of the parameters can be guaranteed. However, in some cases, such as temperature and other reasons, there will be a certain deviation in the identification results, but the errors are kept within 5% [36]. And since

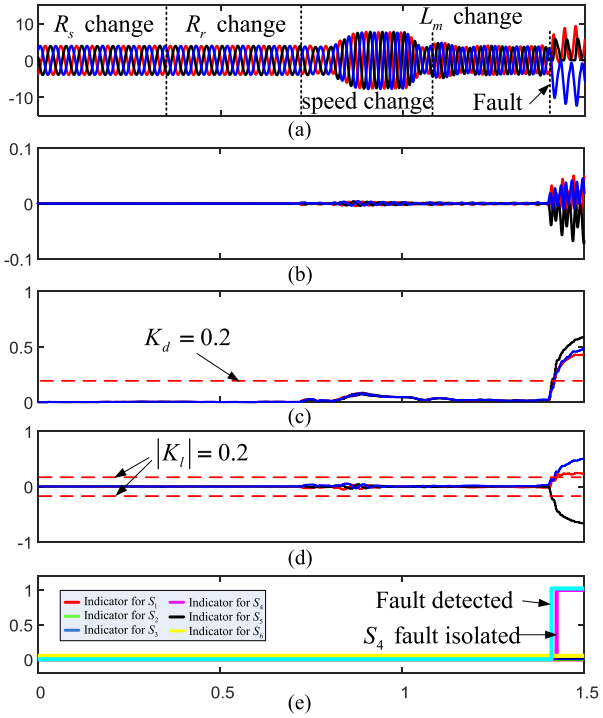

Fig. 12. Simulation results when the motor parameters change.

the temperature has a great influence on the resistance [35], the error of the resistance is set to 10% and the error of the inductance is 5% in this article, and the parameter deviation experiment is carried out.

Fig. 12 shows the simulation result when the motor parameters are incorrect. At the start, the deviation of R_s is set to 10%, and based on the R_s deviation, R_r is set to 10% from the normal value at 0.3 s. Then, based on the previous changes, L_m also deviates by 5% at 0.7 s. The speed and load are changed at 0.9 s. Finally, the S_4 OC fault occurred at 1.4 s.

From Fig. 12, when the motor parameters change, the deviation of the parameters does affect the identification accuracy of the flux and rotational speed. Under normal conditions, the error voltage does have a certain fluctuation. Especially when the speed and torque change, the voltage error fluctuates greatly. However, its fluctuations are much smaller compared to that in the faulty condition. Therefore, the proposed method can also diagnose and locate faults when the motor parameters are inaccurate. If the margin between $\bar{Q}^p$ and the threshold is considered to be small, the value of K_d can be changed and set to $K_d = 0.5$ or above, that is, four times the maximum value of the error voltage. Compared with other simulations and experiments, it can be seen that $K_d = 0.5$ does not affect the fault diagnosis in other states. Therefore, the deviation of the parameters within a certain range does not affect the accuracy of the proposed method.

Through the simulation, the proposed diagnosis method can accurately diagnose the faulty switch in the SVC system, and there is no misdiagnosis when the load torque and the speed changes or the parameters are inaccurate. The detect time can reach about $T/4$.

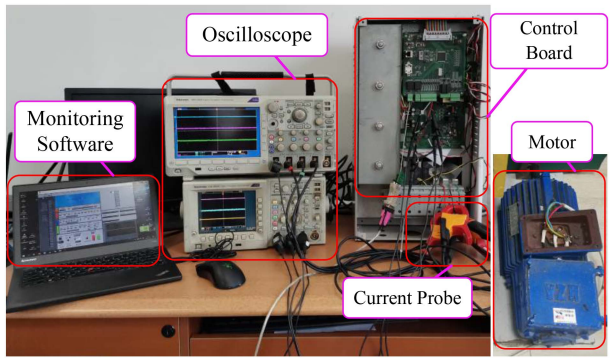

Fig. 13. Experimental platform.

B. Experiment Analysis

In order to verify the correctness of the proposed method, a set of experimental platform based on the two-level topology is set up in the laboratory, as shown in Fig. 13. The SVC control system is based on Altera's FPGA EP4CE10E22C8. Equation (15) is used as the activation function. The sampling frequency is $f_s = 10$ kHz. The load is a 2.2-kW induction motor, with 50-Hz rated frequency and 380-V rated voltage.

1) Fault Diagnosis When Load and Speed Changes: Fig. 14 shows the experimental waveform when load and speed change. The reference frequency is 15 Hz. Then, $N = 600$, $n = 20$, and $m = 1$. In Fig. 14(a), the upper part is the three-phase currents, and the lower part is $\Delta u_{\text{comp\_}\alpha}$ and $\Delta u_{\text{comp\_}\beta}$, which is outputted by the D/A conversion circuit. In Fig. 14(b) is e^p. Fig. 14(c) and (d) shows the absolute feature function and the feature function. Fig. 14(e) shows the detection and isolation results. From Fig. 14, the speed change also causes torque changes. But none of them caused the e^p to change. e^p always fluctuates around 0, and its feature function $\bar{Q}^p$ does not exceed the control line K_d. Therefore, no fault occurred.

2) Fault Diagnosis When Fault Occurs: Fig. 15 shows the experimental waveform for the OC fault of S_1 in the given phase A. The waveform shown in the subgraph is the same as Fig. 14. The frequency is 50 Hz. So $N = 200$, $n = 20$, and $m = 1$. The results are calculated by the proposed fault diagnosis method same to the simulation. It can be seen from the results that the proposed method can accurately locate the fault IGBT when the fault occurs. Moreover, due to the SOMMF, the fault can be accurately located within a few sampling cycles after the fault happens. The timeliness and accuracy of the algorithm are verified. Therefore, experiments verify the effectiveness of the proposed method.

3) Fault Occurs When Speed and Load Change: Fig. 16 shows the experimental waveform for the OC fault of S_2 in the given phase A. The waveform shown in the subgraph is the same as Fig. 14. In this case, $N = 600$, $n = 20$, and $m = 1$. As can be seen from Fig. 16, when the speed and load change, the error voltage fluctuates very little. However, the error voltage fluctuates greatly when an OC fault occurs. It can be seen that although the period of the error voltage changes, the exact signal period is no longer required due to the use of the activation function. Moreover, due to the SOMMF, the fault can be accurately

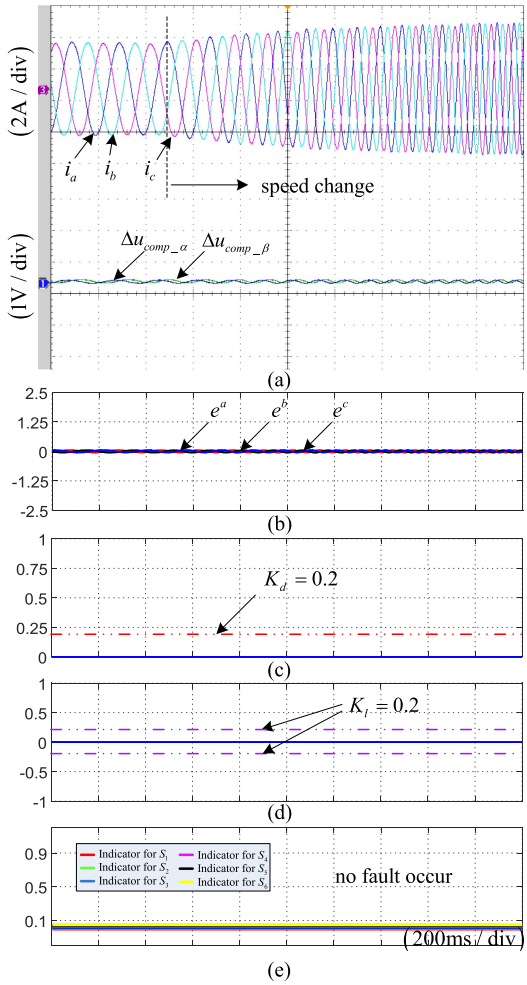

Fig. 14. Experimental results of speed and load variation. (a) Three-phase currents and the error voltages. (b) Three-phase error voltages. (c) Absolute feature function. (d) Feature function. (e) Detection and isolation results.

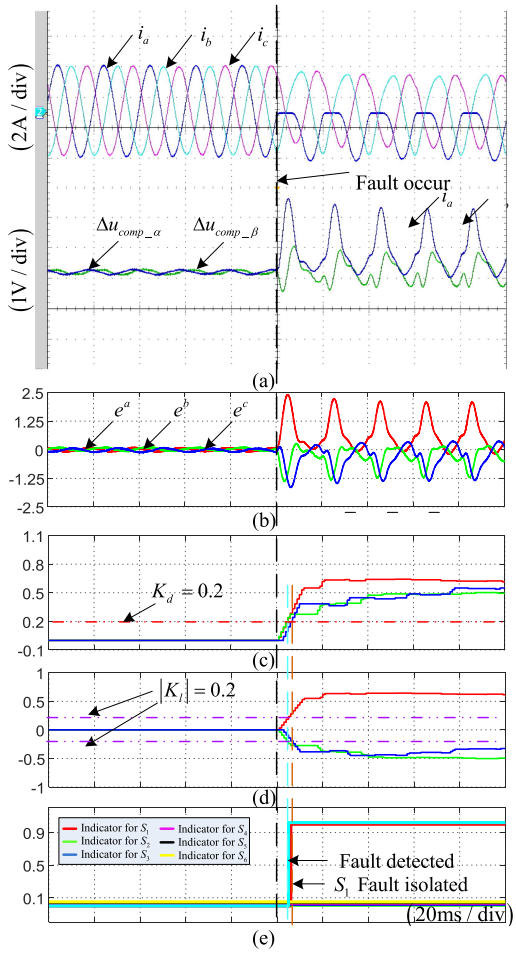

Fig. 15. Experimental results of S_1 open-circuit fault in phase A. (a) Three-phase currents and the error voltages. (b) Three-phase error voltages. (c) Absolute feature function. (d) Feature function. (e) Detection and isolation results.

located within a few sampling cycles after the fault happens. Then, $Q^a(k)$ is increased, and $Q^b(k)$ and $Q^c(k)$ are decreased, and E_k^p is triggered. The timeliness and accuracy of the algorithm are verified.

Thus, the S_2 OC fault is accurately detected and isolated. Changes in speed and load do not cause large fluctuations in the error voltage; so they do not affect the correctness of fault diagnosis.

4) Fault Diagnosis When Parameters Changes: Fig. 17 shows the experimental waveform for the OC fault of S_2 in the given phase A when there are deviations in motor parameters. The waveform shown in the subgraph is the same as Fig. 14. In this case, $N = 600$, $n = 20$, and $m = 1$. Similar to the given parameter deviations in the simulation, the deviations of R_s and R_r are given as 10% of normal value, and the deviation of inductance is given as 5% of normal value. In the actual system, if the given deviation is too large, the SVC system cannot be able to operate normally.

From Fig. 17, when motor parameters change, there is indeed a certain fluctuation in the error voltage under normal conditions. Moreover, when the load changes, the fluctuation of the voltage error is also large. However, its fluctuation is still not enough to compare with the fluctuation in the fault state. Therefore, the deviation of the parameters within a certain range does not affect the accuracy of the proposed method. The proposed method can still diagnose and locate faults when the motor parameters are inaccurate. It can be seen from the results that the proposed method can accurately locate the fault IGBT when the motor parameters change.

C. Compared With Other Methods

In order to further verify the performance of the proposed algorithm, it is compared with some relevant methods from several aspects in Table III and Fig. 18.

From Table III, the proposed method for closed-loop systems can quickly diagnose faults within $1/4$ cycle. Compared with other current-based diagnosis methods, such as the period average method [15], Park method [16], etc., the diagnosis time is greatly reduced and it improves the system reliability. Moreover, those methods can cause misdiagnosis when the speed is changed, as shown in Fig. 18(b). The method [29] [see Fig. 18(c)] eliminates misdiagnosis caused by speed changes by

TABLE III
COMPARISON OF THE PROPOSED METHOD WITH OTHER METHODS

Relevant research method	Consider speed variation	Consider load variation	Suitable for closed-loop	Calculation burden per cycle	Add hardware circuit	Dependence of threshold	Diagnosis time
[15], [16]	No	Yes	No	200	No	High	One cycle
[29]	Yes	Yes	Yes	>200	No	High	>1/4 cycle
[17], [22]	-	-	-	>200	Yes	Low	< 1/4 cycle
[24], [26]	No	Yes	Yes	200	No	High	> 1/2 cycle
[30], [31]	Yes	No	Yes	400 ~ 600	No	-	>2−3 cycle
Proposed method	Yes	Yes	Yes	30	No	Low	<1/4 cycle

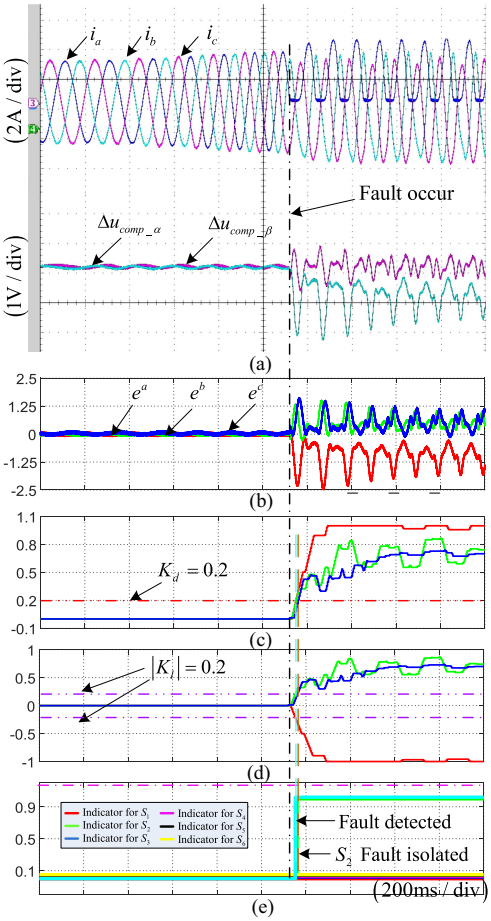

Fig. 16. Experimental results of S_2 OC fault in phase A. (a) Three-phase currents and the error voltages. (b) Three-phase error voltages. (c) Absolute feature function. (d) Feature function. (e) Detection and isolation results.

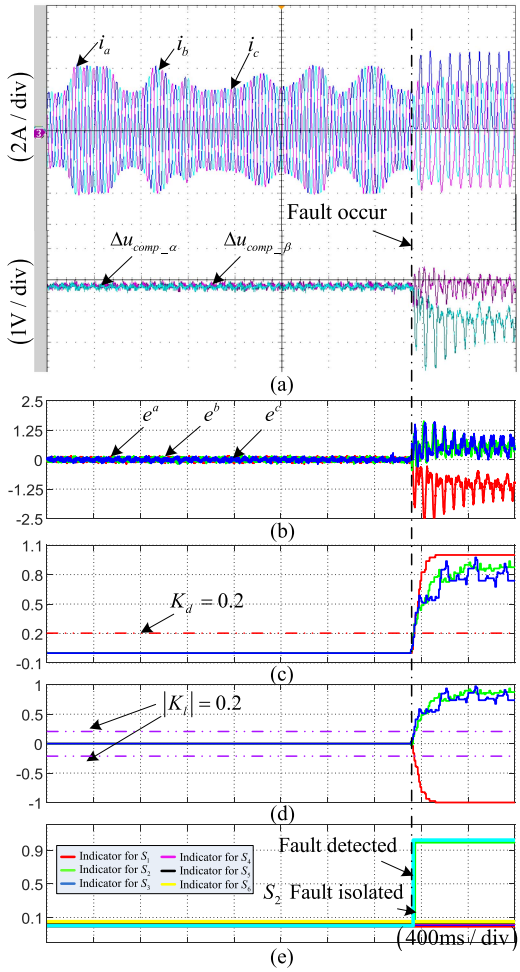

Fig. 17. Experimental results of S_2 OC fault in phase A. (a) Three-phase currents and the error voltages. (b) Three-phase error voltages. (c) Absolute feature function. (d) Feature function. (e) Detection and isolation results.

adding an isotopic function. However, it needs to add multiple thresholds and is very computationally intensive. Therefore, the current-based method requires a long diagnosis time, such as one or several fundamental periods, to ensure high detection accuracy. The voltage-based methods [17], [22] [see Fig. 18(d)] use the error voltage between the estimated voltage and the measured voltage to diagnose faults. Although it has the fastest diagnostic speed and highest accuracy, it requires additional voltage sensors or detection circuits, which increases the cost and points of failure. Compared with [26], [24], [30], and [31], the SOMMF method can reduce the storage of 1-D one-period data from 200 data to at least less than 30, which can make the proposed fault diagnosis method simpler and more efficient. In addition, the knowledge-based method [30], [31] requires a

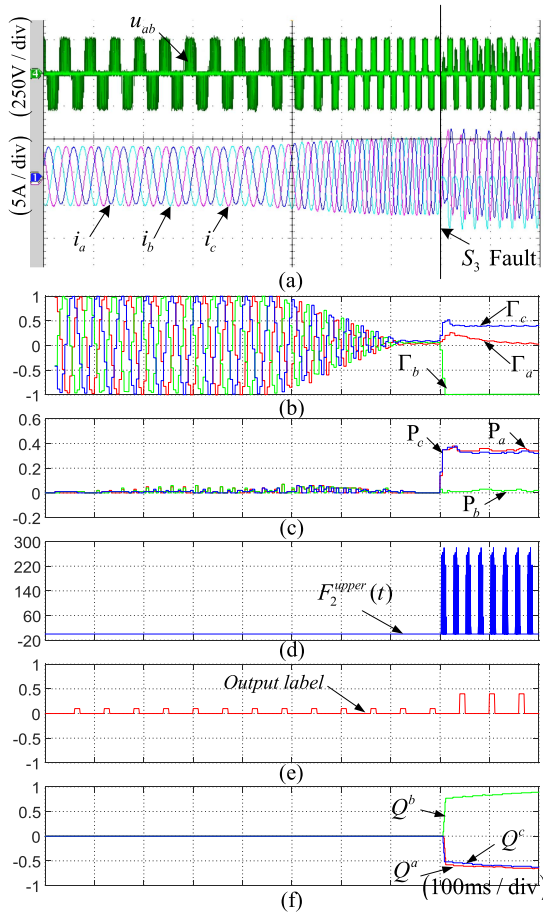

Fig. 18. Comparison of inverter fault diagnosis algorithms. (a) Three-phase currents and the line voltage. (b) Diagnosis variables of [15]. (c) Diagnosis variables of [29]. (d) Diagnosis variables of [17]. (e) Diagnosis variables of [30]. (f) Diagnosis variables of the proposed method.

large amount of historical data for training, which requires a long diagnosis time, as shown in Fig. 18(d). Although the diagnostic accuracy is high, it is difficult to use in the real-time diagnosis process due to its high computational burden.

Furthermore, due to obvious characteristics of fault variables derived from error voltages, the proposed method is not sensitive to the load and speed change and has less computation and shorter fault detection and location time compared with other methods [see Fig. 18(f)].

V. Conclusion

This article proposes an IGBT OC fault diagnosis method for VSIs with an SVC system. It uses the error voltage as a diagnostic factor, which is not affected by changes in load and speed. And the activation function is used to separate fault information and normal information, which can accurately diagnose and locate faults. The fault diagnosis unit is independent of the vector control system. So it can be easily implanted into the control algorithm as a subroutine without major modification. Due to SOMMF, the calculation time of the characteristic function is greatly reduced. For example, in the simulation and experiment, it only needs to calculate at least 20 times per fundamental cycle and storage less than 30 values. Through the simulation and experiment, the correctness of the proposed OC fault diagnosis method embedded in the closed-loop SVC system is verified.

References

[1] J. H. Choi, S. Kim, D. S. Yoo, and K. -H. Kim, "A diagnostic method of simultaneous open-switch faults in inverter-fed linear induction motor drive for reliability enhancement," *IEEE Trans. Ind. Electron.*, vol. 62, no. 7, pp. 4065–4077, Jul. 2015.

[2] B. Wu, *High-Power Converters and AC Drives*. Piscataway, NJ, USA: IEEE Press/Wiley-Interscience, 2006.

[3] Y. Han, P. Shen, X. Zhao, and J. M. Guerrero, "An enhanced power sharing scheme for voltage unbalance and harmonics compensation in an islanded microgrid," *IEEE Trans. Energy Convers.*, vol. 31, no. 3, pp. 1037–1050, Sep. 2016.

[4] Y. T. Song and B. S. Wang, "Survey on reliability of power electronic systems," *IEEE Trans. Power Electron.*, vol. 28, no. 1, pp. 591–604, Jan. 2013.

[5] Z. Li et al., "A fast diagnosis method for both IGBT faults and current sensor faults in grid-tied three-phase inverters with two current sensors," *IEEE Trans. Power Electron.*, vol. 35, no. 5, pp. 5267–5278, May 2020.

[6] E. Ribeiro, A. J. M. Cardoso, and C. Boccaletti, "Open-circuit fault diagnosis in interleaved DC-DC converters," *IEEE Trans. Power Electron.*, vol. 29, no. 6, pp. 3091–3102, Jun. 2014.

[7] P. Nuutinen, P. Peltoniemi, and P. Silventoinen, "Short-circuit protection in a converter-fed low-voltage distribution network," *IEEE Trans. Power Electron.*, vol. 28, no. 4, pp. 1587–1597, Apr. 2013.

[8] B. Lu and S. K. Sharma, "A literature review of IGBT fault diagnostic and protection methods for power inverters," *IEEE Trans. Ind. Appl.*, vol. 45, no. 5, pp. 1770–1777, Sep. 2009.

[9] H. Yan, Y. Xu, J. Zou, Y. Fang, and F. Cai, "A novel open-circuit fault diagnosis method for voltage source inverters with a single current sensor," *IEEE Trans. Power Electron.*, vol. 33, no. 10, pp. 8775–8786, Oct. 2018.

[10] W. Sleszynski, J. Nieznanski, and A. Cichowski, "Opentransistor fault diagnostics in voltage-source inverters by analyzing the load currents," *IEEE Trans. Ind. Electron.*, vol. 56, no. 11, pp. 4681–4688, Nov. 2009.

[11] Z. Huang and Z. Wang, "A multiswitch open-circuit fault diagnosis of microgrid inverter based on slidable triangularization processing," *IEEE Trans. Power Electron.*, vol. 36, no. 1, pp. 922–930, Jan. 2021.

[12] Z. Huang and Z. Wang, "A fault diagnosis algorithm for microgrid three-phase inverter based on trend relationship of adjacent fold lines," *IEEE Trans. Ind. Inform.*, vol. 16, no. 1, pp. 267–276, Jan. 2020.

[13] D. U. Campos-Delgado, J. A. Pecina-Sanchez, D. R. Espinoza-Trejo, and E. R. Arce-Santana, "Diagnosis of open-switch faults in variable speed drives by stator current analysis and pattern recognition," *IET Electr. Power Appl.*, vol. 7, no. 6, pp. 509–522, Jul. 2013.

[14] J. O. Estima, N. M. A. Freire, and A. J. M. Cardoso, "Recent advances in fault diagnosis by Parks vector approach," in *Proc. IEEE Workshop Elect. Machines Des. Control Diagnosis*, 2013, pp. 279–288.

[15] Z. Jian-Jian, C. Yong, C. Zhang-Yong, and Z. Anjian, "Open-switch fault diagnosis method in voltage-source inverters based on phase currents," *IEEE Access*, vol. 7, pp. 63619–63625, 2019.

[16] H. Zhao and L. Cheng, "Open-switch fault-diagnostic method for back-to-back converters of a doubly fed wind power generation system," *IEEE Trans. Power Electron.*, vol. 33, no. 4, pp. 3452–3461, Apr. 2018.

[17] C. Shu, C. Ya-Ting, Y. Tian-Jian, and W. Xun, "A novel diagnostic technique for open-circuited faults of inverters based on output line-to-line voltage model," *IEEE Trans. Ind. Electron.*, vol. 63, no. 7, pp. 4412–4421, Jul. 2016.

[18] Q. An, L. Sun, K. Zhao, and L. Sun, "Switching function model-based fast-diagnostic method of open-switch faults in inverters without sensors," *IEEE Trans. Power Electron.*, vol. 26, no. 1, pp. 587–593, Jan. 2011.

[19] L. M. A. Caseiro and A. M. S. Mendes, "Real-time IGBT open-circuit fault diagnosis in three-level neutral-point-clamped voltage-source rectifiers based on instant voltage error," *IEEE Trans. Ind. Electron.*, vol. 62, no. 3, pp. 1669–1678, Mar. 2015.

[20] B. Cai, Y. Zhao, H. Liu, and M. Xie, "A data-driven fault diagnosis methodology in three-phase inverters for PMSM drive systems," *IEEE Trans. Power Electron.*, vol. 32, no. 4, pp. 5590–5600, Jul. 2017.

[21] Y. Yu and S. Pei, "Open-circuit fault diagnosis of NeutralPoint clamped three-level inverter based on sparse representation," *IEEE Access*, vol. 6, pp. 2169–3536, 2018.
[22] S. Ahmadi, P. Poure, S. Saadate, and D. A. Khaburi, "A real-time fault diagnosis for neutral-point-clamped inverters based on failure-mode algorithm," *IEEE Trans. Ind. Inform.*, vol. 17, no. 2, pp. 1100–1110, Feb. 2021.
[23] Z. Li, H. Ma, Z. Bai, Y. Wang, and B. Wang, "Fast transistor open-circuit faults diagnosis in grid-tied three-phase VSIs based on average bridge arm pole-to-pole voltages and error-adaptive thresholds," *IEEE Trans. Power Electron.*, vol. 33, no. 9, pp. 8040–8051, Sep. 2018.
[24] D. R. Espinoza-Trejo, D. U. Campos-Delgado, G. Bossio, E. Barcenas, J. E. Hernandez-Diez, and L. F. Lugo-Cordero, "Fault diagnosis scheme for open-circuit faults in field-oriented control induction motor drives," *IET Power Electron.*, vol. 6, pp. 869–877, 2013.
[25] D. U. Campos-Delgado and D. R. Espinoza-Trejo, "An observer-based diagnosis scheme for single and simultaneous open-switch faults in induction motor drives," *IEEE Trans. Ind. Electron.*, vol. 58, no. 2, pp. 671–679, Feb. 2011.
[26] I. Jlassi, J. O. Estima, S. K. El Khil, N. M. Bellaaj, and A. J. M. Cardoso, "A robust observer-based method for IGBTs and current sensors fault diagnosis in voltage-source inverters of PMSM drives," *IEEE Trans. Ind. Appl.*, vol. 53, no. 3, pp. 2894–2905, May/Jun. 2017.
[27] M. A. Masrur, Z. Chen, B. Zhang, and Y. Lu Murphey, "Model-based fault diagnosis in electric drive inverters using artificial neural network," in *Proc. IEEE Power Eng. Soc. Gen. Meeting*, Tampa, FL, USA, 2007, pp. 1–7.
[28] J. Zhang, J. Zhao, D. Zhou, and C. Huang, "High performance fault diagnosis in PWM voltage-source inverters for vector controlled induction," *IEEE Trans. Power Electron.*, vol. 29, no. 11, pp. 6087–6099, Nov. 2014.
[29] F. Wu and J. Zhao, "A real-time multiple open-circuit fault diagnosis method in voltage-source-inverter fed vector controlled drives," *IEEE Trans. Power Electron.*, vol. 31, no. 2, pp. 1425–1437, Feb. 2016.
[30] Y. Xia and Y. Xu, "A transferrable data-driven method for IGBT open-circuit fault diagnosis in three-phase inverters," *IEEE Trans. Power Electron.*, vol. 36, no. 12, pp. 13478–13488, Dec. 2021.
[31] B. Gou, Y. Xu, Y. Xia, Q. Deng, and X. Ge, "An online data-driven method for simultaneous diagnosis of IGBT and current sensor fault of three-phase PWM inverter in induction motor drives," *IEEE Trans. Power Electron.*, vol. 35, no. 12, pp. 13281–13294, Dec. 2020.
[32] S. V. Hule, R. Bindu, and D. Vincent, "Sensorless vector control of three phase induction motor," in *Proc. Int. Conf. Adv. Commun. Comput. Technol.*, Mumbai, India, 2014, pp. 1–6.
[33] N. Diao, X. Sun, C. Song, and H. Zhang, "FPGA-based short horizon integration voltage reconstruction method for three level neutral point clamped inverter," *IEEE Trans. Ind. Electron.*, vol. 68, no. 11, pp. 10412–10421, Nov. 2021.
[34] C. Lascu, I. Boldea, and F. Blaabjerg, "A modified direct torque control for induction motor sensorless drive," *IEEE Trans. Ind. Appl.*, vol. 36, no. 1, pp. 122–130, Jan./Feb. 2000.
[35] S. Yang, D. Ding, X. Li, Z. Xie, X. Zhang, and L. Chang, "A novel online parameter estimation method for indirect field oriented induction motor drives," *IEEE Trans. Energy Convers.*, vol. 32, no. 4, pp. 1562–1573, Dec. 2017.
[36] S. A. Odhano, A. Cavagnino, R. Bojoi, and A. Tenconi, "Induction motor magnetizing characteristic identification at standstill with single-phase tests conducted through the inverter," in *Proc. IEEE Int. Electric Machines Drives Conf.*, 2015, pp. 960–966.
[37] S. A. Odhano, A. Boglietti, R. Bojoi, and E. Armando, "Unified direct-flux vector control of induction motor self-commissioning drive with analysis of parameter detuning effects," in *Proc. IEEE Energy Convers. Congr. Expo.*, 2013, pp. 2071–2078.

Naizhe Diao (Member, IEEE) received the B.S. degree in automation from the Beijing University of Posts and Telecommunications (BUPT), Beijing, China, in 2007, and the M.S. degree in power system and automation and the Ph.D. degree in control theory and control engineering from Northeastern University, Shenyang, China, in 2014 and 2022, respectively.

He is currently a Lecturer with the College of Electrical Engineering, Yanshan University, Qinhuangdao, China. His research interests include electric machines and drives, power electronics, and fault diagnosis.

Yingwei Zhang (Senior Member, IEEE) received the double B.S. degree in automation and mathematics from the Harbin Institute of Technology, Harbin, China, in 1993, and the master's and Ph.D. degrees in control theory and control engineering from Northeastern University, Shenyang, China, in 1998 and 2000, respectively.

She was a Postdoctoral Researcher with Northeastern University from 2001 to 2003 and was promoted to Associate Professor in 2002. Since 2010, she has been a Professor with the State Laboratory of Synthesis Automation of Process Industry, Northeastern University. Her current research interests include modeling, fault detection, and diagnosis.

Dr. Zhang won the National Science Fund for Distinguished Young Scholars in 2013.

Xianrui Sun (Graduate Student Member, IEEE) received the M.S. degree in power electronics and electrical drives from Northeastern University, Shenyang, China, in 2013. He is currently working toward the Ph.D. degree in electrical engineering with the College of Information Science and Engineering, Northeastern University.

His Ph.D. topic is supported by Promotion China Ph.D. Programme, BMW Brilliance Automotive Ltd., Shenyang, China. His research interests include simulation power battery design, battery management system, and battery state estimation.

Chonghui Song (Member, IEEE) received the B.S. degree in fluid machine engineering from Xi'an Jiaotong University, Xi'an, China, in 1996, and the M.S. and Ph.D. degrees in automatic control theory and engineering from Northeastern University, Shenyang, China, in 1999 and 2004, respectively.

From 2006 to 2008, he was a Visiting Scholar with the Department of Electrical and Computer Engineering, University of Illinois at Chicago, Chicago, IL, USA. He is currently an Associate Professor with the College of Information Science and Engineering, Northeastern University. His current research interests include power electronics, multilevel converters, differential game, optimal control, and dynamic programming.

Wenwen Wang received the B.S. degree in electrical engineering from the Xuzhou University of Technology, Xuzhou, China, in 2019, and the M.S. degree in electrical engineering from Northeastern University, Shenyang, China, in 2022.

Her current research interests include soft switching techniques and high performance inverters.

Haifeng Zhang (Student Member, IEEE) received the M.S. degree in biomedical engineering in 2019 from Northeastern University, Shenyang, China, where he is currently working toward the Ph.D. degree in control science and engineering with the College of Information Science and Engineering.

His research interests include machine learning, pattern recognition, and fault diagnosis.